Efficient prediction of airborne noise propagation in a non-turbulent urban environment using Gaussian beam tracing method

Yunus, Furkat; Casalino, Damiano; Avallone, Francesco; Ragni, Daniele

DOI
10.1121/10.0017825

Publication date
2023

Document Version
Final published version

Published in
Journal of the Acoustical Society of America

APRIL 19 2023

Efficient prediction of airborne noise propagation in a non-turbulent urban environment using Gaussian beam tracing method

Furkat Yunus; Damiano Casalino; Francesco Avallone; ... et. al

J Acoust Soc Am 153, 2362 (2023)
https://doi.org/10.1121/10.0017825

JASA ARTICLE

Efficient prediction of airborne noise propagation in a non-turbulent urban environment using Gaussian beam tracing method

Furkat Yunus,[1,a] Damiano Casalino,[1] Francesco Avallone,[2] and Daniele Ragni[1]
[1]*Flow Physics and Technology Department, Delft University of Technology, Delft 2629HS, The Netherlands*
[2]*Department of Mechanical and Aerospace Engineering, Politecnico di Torino, 10129, Torino, Italy*

ABSTRACT:
This paper presents a noise propagation approach based on the Gaussian beam tracing (GBT) method that accounts for multiple reflections over three-dimensional terrain topology and atmospheric refraction due to horizontal and vertical variability in wind velocity. A semi-empirical formulation is derived to reduce truncation error in the beam summation for receivers on the terrain surfaces. The reliability of the present GBT approach is assessed with an acoustic solver based on the finite element method (FEM) solutions of the convected wave equation. The predicted wavefields with the two methods are compared for different source-receiver geometries, urban settings, and wind conditions. When the beam summation is performed without the empirical formulation, the maximum difference is more than 40 dB; it drops below 8 dB with the empirical formulation. In the presence of wind, the direct and reflected waves can have different ray paths than those in a quiescent atmosphere, which results in less apparent diffraction patterns. A 17-fold reduction in computation time is achieved compared to the FEM solver. The results suggest that the present GBT acoustic propagation model can be applied to high-frequency noise propagation in urban environments with acceptable accuracy and better computational efficiency than full-wave solutions.
 https://doi.org/10.1121/10.0017825
(Received 12 October 2022; revised 22 March 2023; accepted 24 March 2023; published online 19 April 2023)
[Editor: Vladimir E Ostashev] Pages: 2362–2375

I. INTRODUCTION

Accurate prediction of noise propagation in an urban environment is challenging as various wave phenomena, i.e., multiple reflections, diffraction, refraction, and propagation scenarios, such as standing waves with large amplitude oscillations in narrow urban canyons and scattering by atmospheric turbulence, should be accounted for. Over the years, computational tools have been developed to simulate outdoor noise propagation. The fast field program (FFP) (Franke and Swenson, 1989; Raspet *et al.*, 1985; Salomons, 2001; Wilson, 1993) and the parabolic equation (PE) (Gilbert and Di, 1993; Gilbert and White, 1989; Hornikx, 2004; Ostashev and Wilson, 2015; Salomons, 2001; West *et al.*, 1992) are two of the most popular frequency-domain methods. The FFP, in its standard form, assumes a horizontally stratified propagation medium and a flat and homogeneous ground (Franke and Swenson, 1989; Salomons, 2001) and, thus, cannot be employed for urban environments. The PE is based on a one-way approximation (Ostashev and Wilson, 2015; Salomons, 2001) and neglects backscattering. While PE can handle uneven terrain, the accuracy of PE solutions depends on the radiation angles at the source (Gilbert and Di, 1993; Gilbert *et al.*, 1990; Gilbert and White, 1989; West *et al.*, 1992) and its application to urban environments is rather limited (Doc *et al.*, 2015). On the other hand, methods based on the solution of wave equations using discretized versions of partial differential equations, such as a finite element or finite difference methods, can include complex propagation scenarios in an urban environment. For instance, finite-difference, time-domain (FDTD) methods have been applied to outdoor sound propagation (Ostashev *et al.*, 2005; Wilson and Liu, 2004), including atmospheric refraction due to wind variation (Blumrich and Heimann, 2002; Zheng and Li, 2008) and various ground conditions with varying terrain topology (Cotté and Blanc-Benon, 2009; Dragna *et al.*, 2013; Heimann and Karle, 2006; Oshima *et al.*, 2013). The finite element method (FEM) has been used to estimate the insertion loss of a noise barrier in a city environment (Papadakis and Stavroulakis, 2020), and to simulate helicopter noise in a complex urban setting (Casalino *et al.*, 2011). A different approach consists in solving the compressible Navier-Stokes or lattice-Boltzmann (LB) equation to solve both the acoustic and aerodynamic flow fields in a single simulation. The LB method has been applied to simulate outdoor noise propagation (Alguacil *et al.*, 2022; Salomons *et al.*, 2016) and the noise of emerging urban air mobility (UAM) vehicles in a futuristic urban environment (Casalino *et al.*, 2019). Nevertheless, they are computationally demanding and could be unaffordable when the acoustic impact of high-frequency noise or large propagation distances are considered.

[a]Electronic mail: f.yunus@tudelft.nl

 0001-4966/2023/153(4)/2362/14/$30.00

https://doi.org/10.1121/10.0017825

Contrary to the methods mentioned previously, ray-tracing is a widely used approach for studying high-frequency, long-range sound propagation in a complex environment. Ray-tracing has been shown to provide comparable results to wave-based methods for many high-frequency sound propagation problems. Yet, it has limitations such as singularities in perfect shadow zones and caustics (Ostashev and Wilson, 2015; Salomons, 2001). The shadow zone typically appears in an upward refracting atmosphere where the source-receiver range is several times longer than the source height. Ray-tracing predicts zero amplitude in the shadow zone with a sharp discontinuity at the shadow boundary (perfect shadow zone); it predicts an infinite amplitude at locations where the ray tube cross section area vanishes (caustics).

Gaussian beam tracing (GBT), a high-frequency approximate solution of the wave equation, is a widely used approach in seismology and ocean acoustics for studying wave propagation in a complex environment. As pointed out by several authors (Gabillet *et al.*, 1993; Porter, 2019; Porter and Bucker, 1987), the beam tracing has two remarkable advantages over classical ray tracing. First, beams smooth out singularities at caustics and shadow boundaries, thus providing more accurate results; second, it is more efficient if receivers distributed over a vast area are considered instead of a single point because eigenrays connecting the source and the receivers do not need to be identified. Gabillet *et al.* (1993) developed a two-dimensional (2D) version of the GBT method and applied it for sound propagation in the atmosphere for the first time. The work, however, did not investigate multiple reflections over irregular surfaces and the impact of range-dependent terrain topology on acoustic propagation. The urban canyon (UC), also known as the U-shaped street canyon, represents a typical modern dense high-rise city environment and highly distorts wind velocity and temperature profiles. Therefore, complex propagation scenarios could occur during sound propagation, such as standing waves with large amplitude oscillations within a narrow UC (Pelat *et al.*, 2009) and insonification of terrain shadow zone with downward refraction (Hornikx *et al.*, 2018). Another limitation of the work, which has not been pointed out by others yet, is that the authors presented the ray-path-tracing (RPT) equations and the GBT equations in a slightly inconsistent way. The RPT equations explicitly include wind velocity and its gradients suitable for RPT in an atmosphere that is inhomogeneous in temperature or density distribution and moving due to wind velocity. In contrast, the GBT equations do not contain any term related to wind velocity and its gradients; they are only valid in an inhomogeneous quiescent medium. As demonstrated in their work, the 2D GBT model can handle weak refraction due to vertical variation in the wind velocity that is analogous to the variation in the air temperature. Nevertheless, in the presence of strong refraction due to wind velocity variations, the GBT prediction deviated up to 10 dB from the experimentally measured results. Recently, several GBT tools (Bian *et al.*, 2020, 2021; Bian *et al.*, 2022; Mo *et al.*, 2017) have been developed and applied to atmospheric acoustic propagation problems. Although these tools are efficient in RPT, they cannot account for atmospheric refraction due to horizontal or vertical variability in the wind velocity in a three-dimensional (3D) environment. This is because both the RPT and the GBT formulations presented in these works are derived for GBT in an inhomogeneous quiescent medium.

Applying the GBT method to atmospheric sound propagation poses another intrinsic difficulty that arises when the wavefield is predicated on the terrain surfaces only. Namely, when the beams interact with the terrain boundary, the bottom end of the beam that grazes the terrain boundary passes below the boundary surface, causing spurious truncation error in the wavefield calculation (Bian *et al.*, 2020, 2021; Gabillet *et al.*, 1993). To overcome this intrinsic limitation, Gabillet *et al.* (1993) used large beams and introduced an *ad hoc* scale factor in the wavefield calculation that accounts for the reflected wavefield. Their model, however, failed to produce a more general approach to eliminate the spurious truncation in the wavefield calculation. Despite the severity of this issue, recent publications did not address it. Those GBT models were validated either against some benchmark cases in ocean acoustics (Bian *et al.*, 2020; Mo *et al.*, 2017) or on elevated surfaces in an outdoor environment where the surface height is a few times larger than the acoustic wavelength (Bian *et al.*, 2020).

For an elevated source in a realistic urban environment, vertical and horizontal variabilities in urban topology and weather conditions, two new methodological modifications in the previously-mentioned prediction models are needed: (i) the formulations derived for the GBT in an inhomogeneous moving medium must be used to account for the wind effect on the acoustic propagation; (ii) reflected wavefields on the terrain surfaces should be accounted for with an appropriate approach that eliminates the truncation error in the beam summation on the terrain boundary. The objective of this paper is to include these effects with a new propagation model based on the GBT, apply it for noise prediction in an urban environment, and discuss the physical improvements. The GBT approach adopted in this work is based on well-established RPT (Ostashev and Wilson, 2015) and GBT formulations (Červený and Pšenčík, 2010) developed for studying sound wave propagation in an inhomogeneous moving medium whose description is beyond the scope of the present work. However, they have never been combined and structured as presented in this work for acoustic propagation in an inhomogeneous moving atmosphere. For instance, the RPT in an inhomogeneous moving atmosphere is widely known (Chessell, 1973; Ostashev and Wilson, 2015; Pierce, 2019; Uginčius, 1972), while the GBT in an inhomogeneous moving medium has not been adapted and applied for atmospheric acoustic propagation.

The remainder of this paper is structured as follows. In Sec. II, the methodology is described. Section III evaluates the GBT-based atmospheric acoustic propagation approach within a validation case study. Finally, the summary of the work is given in Sec. IV.

To express the equations concisely, both the component and matrix notation for vectors and matrices are used in this paper. In the component notation, the upper-case indices $(I, J, K, \ldots)$ take the values from 1 to 2, and the lower-case indices $(i, j, k, \ldots)$ the values from 1 to 3. In addition, the Einstein summation convention is used. Bold symbols denote the matrices and vectors. The vectors are considered column matrices. Hence, the scalar product of vectors $\boldsymbol{a}$ and $\boldsymbol{b}$, for instance, reads $\boldsymbol{a}^T\boldsymbol{b}$, the dyadic reads $\boldsymbol{a}\boldsymbol{b}^T$.

II. METHODOLOGY

A standard hybrid methodology is used to predict airborne noise propagation in a 3D urban environment. An in-house solver acoustic ray and Gaussian beam tracer (UYGUR) is developed based on the 3D RPT method (Ostashev and Wilson, 2015) and the GBT method (Červený and Pšenčík, 2010). A schematic illustration of the computational procedures is shown in Fig. 1. The terrain geometry and the 3D wind and temperature profiles are provided as inputs. After reading the environmental profiles, UYGUR calculates the noise propagation in an urban environment in the following steps. In the first step, RPT (Ostashev and Wilson, 2015) is carried out to determine the central ray Ω associated with each Gaussian beam. In the second step, dynamic ray tracing (DRT) (Červený and Pšenčík, 2010) is performed to calculate the geometrical spreading and wavefront variation of the sound wave in the vicinity of each ray. Finally, the acoustic field at receiver points is calculated by summing the contribution of each Gaussian beam passing nearby the receiver location. The wavefield at the receivers distributed on the terrain surfaces is calculated by coupling the beam summation with a novel semi-empirical formulation that eliminates the truncation error and accounts for the reflected wavefields. These steps are briefly outlined in the following.

A. RPT

The first step is to determine ray path trajectory of any ray Ω in an inhomogeneous moving atmosphere. When the atmosphere has a constant temperature and is quiescent, an observer sees a wavefront $T(\boldsymbol{x}) = t$ as a surface that moves with speed $c\boldsymbol{n}$, where t is time, c is the sound speed, and $\boldsymbol{n}$ is normal to the wavefront. However, when the air moves with velocity $\boldsymbol{v}$, the wavefront has a local speed equal to $d\boldsymbol{x}/dt = \boldsymbol{v} + c\boldsymbol{n} = \boldsymbol{u}$. Here, both c and $\boldsymbol{v}$ may vary with position and time. Consequently, the ray-path vector $\boldsymbol{x}(t)$ follows the direction of $\boldsymbol{u}$ instead of $\boldsymbol{n}$. The propagation velocity $\boldsymbol{u}$ is also known as group velocity, and the

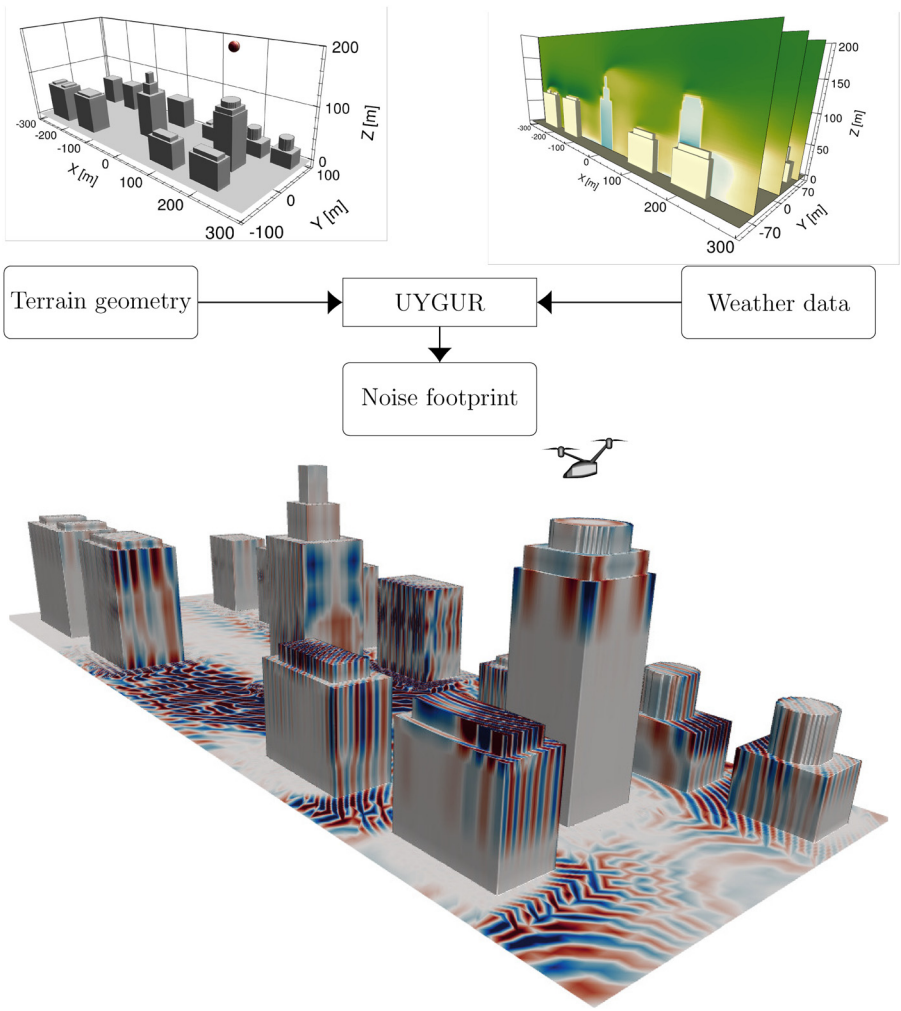

FIG. 1. (Color online) Schematic illustration of the computational procedure.

https://doi.org/10.1121/10.0017825

projection of $\boldsymbol{u}$ in the direction of the normal $\boldsymbol{n}$ equals the magnitude of phase velocity $\mathrm{v} = (\boldsymbol{v}\cdot\boldsymbol{n} + c)\boldsymbol{n}$. Therefore, in an inhomogeneous moving atmosphere $|\mathbf{v}| \le |\boldsymbol{u}|$ and the direction of $\boldsymbol{u}$ is not necessarily the same as that of $\mathbf{v}$.

The ray path can be obtained (Chessell, 1973; Ostashev and Wilson, 2015; Uginčius, 1972) by employing the Hamiltonian formalism that solves the following eikonal equation derived by Pierce (2019):

$$\frac{1}{c} - \frac{\boldsymbol{v}\cdot\nabla T}{c} = |\nabla T|. \tag{1}$$

Equation (1) is a nonlinear first-order partial differential equation, known as the Hamilton-Jacobi equation, that describes the propagation of the acoustic wavefront in an inhomogeneous moving atmosphere. Hence, the equation can be expressed in the form $\mathcal{H}(\boldsymbol{s},\boldsymbol{x}) = |\nabla T| - 1/c + \boldsymbol{v}\cdot\nabla T/c = 0$, where $\mathcal{H}(\boldsymbol{s},\boldsymbol{x})$ is the Hamiltonian and $\boldsymbol{s}$ is the wave-slowness vector $\boldsymbol{s} = \nabla T$. Here, the label "wave-slowness" is applied as $|\boldsymbol{s}|^{-1} = |\mathbf{v}|$ with which the wavefront moves normal to itself. The solution of $\mathcal{H}(\boldsymbol{s},\boldsymbol{x})$ can be represented by a set of the ordinary differential equations

$$\begin{aligned}\frac{d\boldsymbol{x}}{dt} &= c\frac{\partial\mathcal{H}}{\partial\boldsymbol{s}} = \boldsymbol{u} = \frac{\boldsymbol{s}c}{|\boldsymbol{s}|} + \boldsymbol{v},\\ \frac{d\boldsymbol{s}}{dt} &= -c\frac{\partial\mathcal{H}}{\partial\boldsymbol{x}} = \boldsymbol{\eta} = -|\boldsymbol{s}|\nabla c - \boldsymbol{s}\times(\nabla\times\boldsymbol{v}) - (\boldsymbol{s}\cdot\nabla)\boldsymbol{v}.\end{aligned} \tag{2}$$

Equation (2) is the final form of the RPT equation, which is equivalent to the one derived by Pierce (1990, 2019). Equation (2) is solved using a second-order Runge-Kutta scheme with the initial conditions $t = t_0$, $\boldsymbol{x}(t_0) = \boldsymbol{x}_0$, $\boldsymbol{s}(t_0) = \boldsymbol{s}_0$, where t_0 is an arbitrarily chosen initial time, and $\boldsymbol{s}_0 = [\boldsymbol{n}(t)/\mathrm{v}(t)]_{t=t_0}$. A user-defined number of time steps is used to march the solution forward in time. In addition, an adaptive step size strategy is also implemented that makes ray points finer at receiver locations of interest and coarser at other locations. Similar approaches have been introduced and implemented in previous works (Bian *et al.*, 2020; Porter, 2019) to reduce computational cost.

The coordinates $\boldsymbol{x}$ of the points on the ray trajectory and slowness vectors $\boldsymbol{s}$ at these points are obtained by solving Eq. (2). As a by-product of RPT, several other useful quantities can also be determined, which will be needed in the following: the ray-velocity vector $\boldsymbol{u} = d\boldsymbol{x}/dt$, the unit vector $\boldsymbol{t} = \boldsymbol{u}/|\boldsymbol{u}|$ tangent to the ray, the unit vector $\boldsymbol{n} = \boldsymbol{s}/|\boldsymbol{s}|$ perpendicular to the wavefront, the vector $\boldsymbol{\eta} = d\boldsymbol{s}/dt$, which represents the variations of the slowness vector along the ray, the phase velocity $\mathrm{v} = |\mathbf{v}| = |\boldsymbol{s}|^{-1}$. The RPT can be used to compute all the previously-mentioned quantities only on the ray Ω, not in its vicinity (see Fig. 2), which is not sufficient to calculate the Gaussian beams. The reason is that the variation of the beam amplitude along the ray is determined by the paraxial ray field in the vicinity of the ray, not by a single ray. Furthermore, the calculation of the paraxial ray field requires the resolution of the geometrical spreading and complex-valued paraxial travel time in the vicinity of the ray Ω. In order to compute the quantities related to the paraxial ray field, it is essential to augment the RPT with an additional procedure called dynamic ray tracing (DRT).

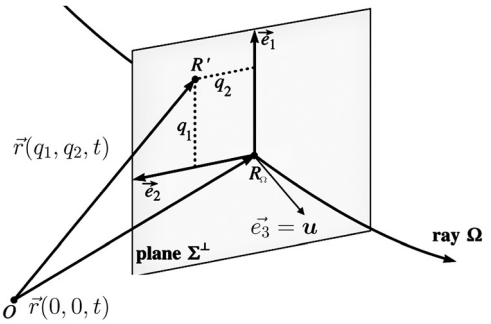

FIG. 2. A field point R' located in the vicinity of a central ray Ω in the ray-centered coordinate system. The field point R' is located on a plane $\Sigma^\perp$ tangent to the wavefront at a point R_Ω on the central ray Ω.

B. DRT

DRT consists of a solution of a system of linear ordinary differential equations of the first order, which can be solved along a ray together with the RPT system or along an existing ray Ω. The solutions of DRT enable one to calculate the travel time in the vicinity of a ray. DRT equations can be expressed in various coordinate systems (ray-centered, Cartesian, etc.). Following Červený and Pšenčík (2010), this paper considers the ray-centered coordinate system $q_i, i = 1,2,3$. Many other details on ray-centered coordinates and DRT in ray-centered coordinates can be found in Klimeš (1994) and Červený (2001).

One of the essential properties of the ray-centered coordinate system is that the central ray Ω represents its coordinate axis q_3. Namely, the coordinate q_3 is defined as a quantity equal to the travel time t along the central ray Ω, $q_3 = t$. The q_1 and q_2 coordinate axes can be introduced as mutually perpendicular straight lines in the plane $\Sigma^\perp$ tangent to the wavefront and intersecting at the central ray Ω as shown in Fig. 2. This property leads to a simple relation between the Cartesian coordinates x_i and the ray-centered coordinates q_j,

$$x_i(q_j) = x_i^\Omega(q_3) + H_{iM}(q_3)q_M, \tag{3}$$

where $i,j = 1,2,3$ and $M = 1, 2$. The central ray Ω is specified by $q_1 = q_2 = 0$, hence, $\boldsymbol{x}(q_1 = 0, q_2 = 0, q_3) = \boldsymbol{x}^\Omega(q_1 = 0, q_2 = 0, q_3)$, where $\boldsymbol{x}^\Omega$ denotes a point on the central ray Ω. The 3×3 transformation matrices $\boldsymbol{H}$ and $\bar{\boldsymbol{H}}$ from ray-centered to Cartesian coordinates and back are defined as $H_{im} = \partial x_i/\partial q_m$ and $\bar{H}_{im} = \partial q_i/\partial x_m$, respectively. In the matrix form, the transformation matrices can be defined as $\boldsymbol{H} = (\boldsymbol{e_1}, \boldsymbol{e_2}, \boldsymbol{e_3} = \boldsymbol{u})$ and $\bar{\boldsymbol{H}}^T = (\boldsymbol{f}_1, \boldsymbol{f}_2, \boldsymbol{f}_3 = \boldsymbol{s})$, where $\boldsymbol{e}_1$, $\boldsymbol{e}_2$, and $\boldsymbol{e}_3$ are the contravariant basis vectors tangential to coordinate axes, whereas $\boldsymbol{f}_1$, $\boldsymbol{f}_2$, and $\boldsymbol{f}_3$ are the covariant basis vectors perpendicular to coordinate surfaces. The basis vectors $\boldsymbol{e}_1$, $\boldsymbol{e}_2$ tangent to the wavefront and $\boldsymbol{e}_3$ tangent to the

central ray Ω are shown in Fig. 2. It should be noted that in moving media, vectors $\boldsymbol{e}_1$ and $\boldsymbol{e}_2$ are not generally perpendicular to $\boldsymbol{u}$. The relation between the transformation matrices $\bar{H}_{ik}H_{kj} = \delta_{ij}$, where δ indicates the Kronecker delta function, can be expressed in terms of $\boldsymbol{e}_i$ and $\boldsymbol{f}_j$ as follows:

$$\boldsymbol{f}_i^T \boldsymbol{e}_j = \delta_{ij}. \tag{4}$$

Equation (4) leads to vectorial relations $\boldsymbol{s}^T\boldsymbol{u} = 1$, $\boldsymbol{s}^T\boldsymbol{e}_I = 0$, and $\boldsymbol{u}^T\boldsymbol{f}_I = 0$. Thus, vectors $\boldsymbol{e}_I$ are perpendicular to the slowness vector $\boldsymbol{s}$, vectors $\boldsymbol{f}_I$ are perpendicular to the group velocity $\boldsymbol{u}$. Equation (4) also yields

$$\begin{aligned} \boldsymbol{f}_1 &= \frac{\boldsymbol{e}_2 \times \boldsymbol{u}}{\boldsymbol{u}^T(\boldsymbol{e}_1 \times \boldsymbol{e}_2)} = \frac{\boldsymbol{e}_2 \times \boldsymbol{u}}{\mathrm{v}}, \\ \boldsymbol{f}_2 &= \frac{\boldsymbol{u} \times \boldsymbol{e}_1}{\boldsymbol{u}^T(\boldsymbol{e}_1 \times \boldsymbol{e}_2)} = \frac{\boldsymbol{e}_1 \times \boldsymbol{u}}{\mathrm{v}}. \end{aligned} \tag{5}$$

The contravariant basis vectors $\boldsymbol{e}_1$ and $\boldsymbol{e}_2$ can be determined by solving an ordinary differential equation of the first order along the central ray Ω,

$$\frac{d\boldsymbol{e}_I}{dt} = -\frac{(\boldsymbol{e}_I^T\boldsymbol{\eta})\boldsymbol{s}}{(\boldsymbol{s}^T\boldsymbol{s})}. \tag{6}$$

Here, $\boldsymbol{s}$ and $\boldsymbol{\eta} = d\boldsymbol{s}/dt$ are known from the RPT. At a selected point t_0 of central ray Ω, initial values for $\boldsymbol{e}_1$ and $\boldsymbol{e}_2$ can be constructed such that they form a triplet of mutually perpendicular unit vectors with $\boldsymbol{n} = \mathrm{v}\boldsymbol{s}$. Based on this, one can ascertain that vectors $\boldsymbol{e}_1$, $\boldsymbol{e}_2$, and $\boldsymbol{n}$ are then right-handed, unit, and mutually perpendicular along the whole central ray Ω. Hence, it is sufficient to calculate only $\boldsymbol{e}_1(t)$ using Eq. (6), as $\boldsymbol{e}_2 = \boldsymbol{n}(t) \times \boldsymbol{e}_1(t)$, and the vectors $\boldsymbol{f}_I$ are determined analytically using Eq. (5), and $\boldsymbol{e}_3 = \boldsymbol{u}$ and $\boldsymbol{f}_3 = \boldsymbol{s}$ are known from the RPT. It is worth highlighting that vectors $\boldsymbol{f}_1$ and $\boldsymbol{f}_2$ may not necessarily be of unit amplitude and mutually perpendicular, but $\boldsymbol{e}_1$ and $\boldsymbol{e}_2$ are.

The DRT system in ray-centered coordinates consists of eight equations for $Q_{IJ} = \partial q_I/\partial\gamma_J$ and $P_{IJ} = \partial p_I/\partial\gamma_J$, with $I, J = 1, 2$. Here, γ_1 and γ_2 are any of the two ray parameters (shooting angles, for instance), p_I denotes the Ith component of the slowness vector $\boldsymbol{s}$ in the ray-centered coordinate system, $p_I = H_{Ik}s_k$. Quantities Q_{IJ} and P_{IJ} $(I, J = 1, 2)$ can be interpreted as the off-ray paraxial changes of q_I and p_I, caused by the changes of γ_I. In matrix form, the DRT system reads

$$\begin{aligned} \frac{d\boldsymbol{Q}}{dt} &= \boldsymbol{A}\boldsymbol{Q} + \boldsymbol{B}\boldsymbol{P}, \\ \frac{d\boldsymbol{P}}{dt} &= -\boldsymbol{C}\boldsymbol{Q} - \boldsymbol{D}\boldsymbol{P}. \end{aligned} \tag{7}$$

All matrices in Eq. (7) are 2×2. The matrices $\boldsymbol{A}$, $\boldsymbol{B}$, $\boldsymbol{C}$, and $\boldsymbol{D}$ are given by relations

$$\begin{aligned} \boldsymbol{A} &= \boldsymbol{f}^T\boldsymbol{A}^{(x)}\boldsymbol{e} + \boldsymbol{d}, \quad \boldsymbol{B} = \boldsymbol{f}^T\boldsymbol{B}^{(x)}\boldsymbol{f}, \\ \boldsymbol{C} &= \boldsymbol{e}^T(\boldsymbol{C}^{(x)} - \boldsymbol{\eta}\boldsymbol{\eta}^T)\boldsymbol{e}, \quad \boldsymbol{D} = \boldsymbol{e}^T\boldsymbol{D}^{(x)}\boldsymbol{f} + \boldsymbol{d}^T. \end{aligned} \tag{8}$$

The 3×3 matrices $\boldsymbol{A}^{(x)}$, $\boldsymbol{B}^{(x)}$, $\boldsymbol{C}^{(x)}$, and $\boldsymbol{D}^{(x)}$ are defined in terms of Cartesian derivatives of the Hamiltonian,

$$\begin{aligned} A_{ij}^{(x)} &= \frac{\partial^2\mathcal{H}}{\partial s_i \partial x_j}, \quad B_{ij}^{(x)} = \frac{\partial^2\mathcal{H}}{\partial s_i \partial s_j}, \\ C_{ij}^{(x)} &= \frac{\partial^2\mathcal{H}}{\partial x_i \partial x_j}, \quad D_{ij}^{(x)} = \frac{\partial^2\mathcal{H}}{\partial x_i \partial s_j}. \end{aligned} \tag{9}$$

Note that $D_{ij}^{(x)} = A_{ji}^{(x)}$. The 3×2 matrix $\boldsymbol{e}$ is comprised of two-unit basis vectors, tangent to the wavefront: $\boldsymbol{e} = (\boldsymbol{e}_1, \boldsymbol{e}_2)$. The 3×2 matrix $\boldsymbol{f} = (\boldsymbol{f}_1, \boldsymbol{f}_2)$ composed of two covariant basis vectors $\boldsymbol{f}_1$ and $\boldsymbol{f}_2$, perpendicular to the ray, can be determined using Eq. (5). The 2×2 matrix $\boldsymbol{d}$ is defined as $\boldsymbol{d} = \boldsymbol{f}^T d\boldsymbol{e}/dt$, where the derivative $d\boldsymbol{e}/dt$ is given by Eq. (6). Numerically, the most time consuming procedure in DRT in ray-centered coordinates in an inhomogeneous moving medium is the determination of the 3×3 matrices $\boldsymbol{A}^{(x)} \equiv \boldsymbol{D}^{(x)T}$, $\boldsymbol{B}^{(x)}$, and $\boldsymbol{C}^{(x)}$ (Červený and Pšenčík, 2010).

Once a ray interacts with solid boundaries like irregular ground surfaces, it is essential to introduce the conditions for the DRT along central rays of reflected or transmitted waves at the point of incidence. At the point of incidence, this is achieved by the continuity property of $\boldsymbol{Q}$ and $\boldsymbol{P}$ that reads

$$\begin{pmatrix} \tilde{\boldsymbol{P}} \\ \tilde{\boldsymbol{Q}} \end{pmatrix} = \Pi(\tilde{t_\Sigma}, t_\Sigma) \begin{pmatrix} \boldsymbol{P} \\ \boldsymbol{Q} \end{pmatrix}, \tag{10}$$

where $\Pi(\tilde{t_\Sigma}, t_\Sigma)$ is 4×4 matrix known as the interface propagator matrix that is given by the relation

$$\Pi(\tilde{t_\Sigma}, t_\Sigma) = \begin{bmatrix} \tilde{\boldsymbol{K}}^T\boldsymbol{K}^{-T} & \boldsymbol{0} \\ \tilde{\boldsymbol{K}}^{-1}[\boldsymbol{E} - \tilde{\boldsymbol{E}} - (\sigma - \tilde{\sigma})\boldsymbol{D}]\boldsymbol{K}^{-T} & \tilde{\boldsymbol{K}}^{-1}\boldsymbol{K} \end{bmatrix}. \tag{11}$$

Detailed derivation of Eq. (10) can be found in Červený and Moser (2007). In Eqs. (10) and (11) and hereafter, the symbols without a tilde correspond to the point of incidence, $t = t_\Sigma$, while the symbols with a tilde correspond to the point of reflection or transmission, $t = \tilde{t_\Sigma}$. As the explanation of symbols with and without tilde is analogous, here, only the symbols corresponding to the point of incidence t_Σ are presented.

Let Σ be a solid boundary that separates the terrain surface from the air. The parametric description of the boundary can be given by relations $\boldsymbol{x} = \boldsymbol{g}(w_1, w_2)$ where $w_I, I = 1, 2$, are the Gaussian coordinates of the surface. The Gaussian coordinates w_1 and w_2, as a special case, can also be considered as the local Cartesian coordinates in a plane tangent to interface Σ at the point of incidence $t = t_\Sigma$ of the central ray Ω. In the vicinity of the point of incidence, the interface can be approximated to the second order in w_I by the relation

$$\boldsymbol{x}(w_I) = \boldsymbol{x}_{inc} + \boldsymbol{g}_I w_I + \frac{1}{2}\boldsymbol{g}_{IJ} w_I w_J. \tag{12}$$

Here, $\boldsymbol{g}_J = \partial\boldsymbol{g}/\partial w_J$ are vectors tangent to Σ at $\boldsymbol{x} = \boldsymbol{x}_{inc}$, and $\boldsymbol{g}_{IJ} = \partial^2\boldsymbol{g}/\partial w_I \partial w_J$ are related to the curvature of the interface at $\boldsymbol{x} = \boldsymbol{x}_{inc}$. More details can be found in (Červený and Moser, 2007; Moser and Červený, 2007). The vectors

https://doi.org/10.1121/10.0017825

$\boldsymbol{g}_J$ are, in general, neither of unit amplitude nor mutually perpendicular. The unit normal vector to the interface $\boldsymbol{N}$ is defined as $\boldsymbol{N} = \boldsymbol{g}_1 \times \boldsymbol{g}_2/|\boldsymbol{g}_1 \times \boldsymbol{g}_2|$. The 2×2 matrices $\boldsymbol{K}$ and $\boldsymbol{K}^{-1}$ in Eq. (11) are given by relations

$$\boldsymbol{K} = (\boldsymbol{g}_1, \boldsymbol{g}_2)^T (\boldsymbol{f}_1, \boldsymbol{f}_2), \quad \boldsymbol{K}^{-1} = (\boldsymbol{e}_1, \boldsymbol{e}_2)^T (\boldsymbol{h}_1, \boldsymbol{h}_2),$$
$$\boldsymbol{h}_1 = \frac{\boldsymbol{g}_2 \times \boldsymbol{u}}{\boldsymbol{u}^T (\boldsymbol{g}_1 \times \boldsymbol{g}_2)}, \quad \boldsymbol{h}_2 = \frac{\boldsymbol{u} \times \boldsymbol{g}_1}{\boldsymbol{u}^T (\boldsymbol{g}_1 \times \boldsymbol{g}_2)}. \tag{13}$$

The 2×2 inhomogeneity matrix $\boldsymbol{E}$ is defined as $E_{IJ} = (\boldsymbol{g}_I^T \boldsymbol{s})(\boldsymbol{e}_K^T \boldsymbol{\eta})(\boldsymbol{g}_J^T \boldsymbol{f}_K) + (\boldsymbol{g}_I^T \boldsymbol{\eta})(\boldsymbol{g}_J^T \boldsymbol{s})$, where $\boldsymbol{s}$ and $\boldsymbol{\eta}$ are calculated from the RPT at the point of incidence. In a homogeneous and motionless atmosphere, $\boldsymbol{E} = \boldsymbol{0}$, as $\boldsymbol{\eta} = \boldsymbol{0}$. The 2×2 curvature matrix $\boldsymbol{D}$ is defined as $D_{IJ} = \boldsymbol{g}_{IJ}^T \boldsymbol{N}$. For a plane interface, $\boldsymbol{D} = \boldsymbol{0}$. The scalars σ and $\tilde{\sigma}$ in Eq. (11) are given by relations $\sigma = \boldsymbol{N}^T \boldsymbol{s}$ and $\tilde{\sigma} = \boldsymbol{N}^T \tilde{\boldsymbol{s}}$. It should be noted that $\boldsymbol{g}_I = \tilde{\boldsymbol{g}}_I$, but $\boldsymbol{e}_I \neq \tilde{\boldsymbol{e}}_I$, $\boldsymbol{f}_I \neq \tilde{\boldsymbol{f}}_I$ and $\boldsymbol{h}_I \neq \tilde{\boldsymbol{h}}_I$. At t_Σ, vectors $\boldsymbol{u}$, $\boldsymbol{s}$ and $\boldsymbol{\eta}$ are known from the RPT. While at $\tilde{t_\Sigma}$, quantities $\tilde{\boldsymbol{u}}$, $\tilde{\boldsymbol{s}}$ and $\tilde{\boldsymbol{\eta}}$ can be calculated using Snell's law (Červený and Moser, 2007; Moser and Červený, 2007).

C. Gaussian beams and wavefield calculation

Once the RPT and DRT systems for a central ray Ω are resolved, the complex pressure contribution from a point R_Ω along the Gaussian beam to the observer point R' situated in the vicinity of the central ray Ω (see Fig. 2) is given by (Červený and Pšenčík, 2010)

$$p^b(R') = P^\Omega \exp\left[-\omega \mathrm{Im}(T(R'))\right] \times \exp\left\{-i\omega\left[t - \mathrm{Re}(T(R'))\right]\right\}, \tag{14}$$

where ω is the angular frequency and P^Ω is given by the relation

$$P^\Omega = A(t_0)\left[\frac{\rho(t_0)\mathrm{v}(t_0)\det \boldsymbol{Q}(t_0)}{\rho(t)\mathrm{v}(t)\det \boldsymbol{Q}(t)}\right]^{1/2} \mathcal{R}^C, \tag{15}$$

where ρ is the density, $\mathcal{R}^C$ is the complete energy reflection/transmission coefficient, which is a product of wave energy reflection/transmission coefficients determined at all points of incidence of ray Ω on the structural interfaces between t_0 and t. $A(t_0)$ is a scalar amplitude at the source location. The complex-valued paraxial travel time $T(R')$ is given by

$$T(R') = T(R_\Omega) + \left[\boldsymbol{x}(R') - \boldsymbol{x}(R_\Omega)\right]^T \boldsymbol{s}(R_\Omega) + \frac{1}{2}\left[\boldsymbol{x}(R') - \boldsymbol{x}(R_\Omega)\right]^T \boldsymbol{M}^{(x)}(R_\Omega)\left[\boldsymbol{x}(R') - \boldsymbol{x}(R_\Omega)\right]. \tag{16}$$

The elements of 3×3 matrix $\boldsymbol{M}^{(x)}$ are given by $\boldsymbol{M}^{(x)} = f\boldsymbol{M}\boldsymbol{f}^T + \boldsymbol{s}\boldsymbol{\eta}^T + \boldsymbol{\eta}\boldsymbol{s}^T - \boldsymbol{s}\boldsymbol{s}^T(\boldsymbol{u}^T\boldsymbol{\eta})$. Here, $\boldsymbol{M}$ is a 2×2 matrix of the second derivatives of travel time field and defined as $\boldsymbol{M} = \boldsymbol{P}\boldsymbol{Q}^{-1}$. It should be noted that matrix $\boldsymbol{M}$ is a complex-valued symmetric matrix that is determined by solving the DRT system with the initial conditions $\boldsymbol{Q}(t_0) = \boldsymbol{R}$, and $\boldsymbol{P}(t_0) = \boldsymbol{M}_0\boldsymbol{R}$. Here, $\boldsymbol{R}$ is an arbitrary constant real-valued finite 2×2 matrix and $\det \boldsymbol{R} \neq 0$. In this study, an identity matrix, i.e., $\boldsymbol{R} = \boldsymbol{I}$, is considered. The matrix $\boldsymbol{M}_0 = \boldsymbol{M}(t_0) = \boldsymbol{P}(t_0)\boldsymbol{Q}^{-1}(t_0)$ is complex-valued and $\mathrm{Re}(\boldsymbol{M}_0)$ and $\mathrm{Im}(\boldsymbol{M}_0)$ are real valued, symmetric and finite. Furthermore, $\mathrm{Im}(\boldsymbol{M}_0)$ is positive definite, and, generally, $\mathrm{Re}(\boldsymbol{M}_0) = \boldsymbol{0}$.

Finally, the total acoustic pressure at the receiver point R' is obtained by integrating the contributions of all individual Gaussian beams passing near the receiver point,

$$P(R', \omega) = \int\int_{\mathcal{D}} \Phi(\gamma_1, \gamma_2) p^b(R') d\gamma_1 d\gamma_2, \tag{17}$$

where $\mathcal{D}$ is the region of integration over the initial ray parameters γ_1 and γ_2, and $\Phi(\gamma_1, \gamma_2)$ is the weighting function. The weighting function is calculated by expanding the wavefield at the source and matching the high-frequency asymptotic behavior of the integral in Eq. (17) to the exact solution for a source in a homogeneous medium where the ray field is regular. The weighting function is given by (Červený, 2001),

$$\Phi(\gamma_1, \gamma_2) = \frac{\omega}{2\pi}\left[-\det(\boldsymbol{M} - \boldsymbol{M}^a)\right]^{1/2} |\det \boldsymbol{Q}^a|, \tag{18}$$

where the superscript $(\cdot)^a$ indicates terms applied in the actual ray field, and $\boldsymbol{M} \neq \boldsymbol{M}^a$. A necessary condition in the derivation of Eq. (18) is the regularity of the ray field. The ray field is regular on a surface if it covers continuously and uniquely the surface with rays, that is, if one and only one ray passes through any point of the surface (Červený, 2001). Equation (17) can give spurious truncation errors if performed on a receiver surface where the ray field is not regular. The terrain surfaces, for instance, are a typical example of such surfaces where the ray field is not regular. A novel approach is developed in this work to overcome this intrinsic limitation of the GBT method, which will be outlined in the following section.

D. Wavefield on the terrain surfaces

If the wavefield on the terrain surface is calculated using Eq. (17), a truncation error will arise as the regularity condition is violated (Bian *et al.*, 2020, 2021; Gabillet *et al.*, 1993). This error is related to the beam width and becomes more significant when ω decreases. The half-width of a beam reads

$$L(R', \omega) = \left[\frac{2}{\omega}\mathrm{Im}(\boldsymbol{M}^{-1})\right]^{1/2}. \tag{19}$$

At lower frequencies, for instance, the beam width becomes large; therefore, the bottom end of the beam that grazes the terrain boundary passes below the boundary surface (see Fig. 3). To eliminate the truncation error, one must perform the beam summation in a way that does not violate the regularity condition. To this end, this work proposes to lift the receivers $\boldsymbol{x}_r$ on the terrain surface Z_r with an offset d

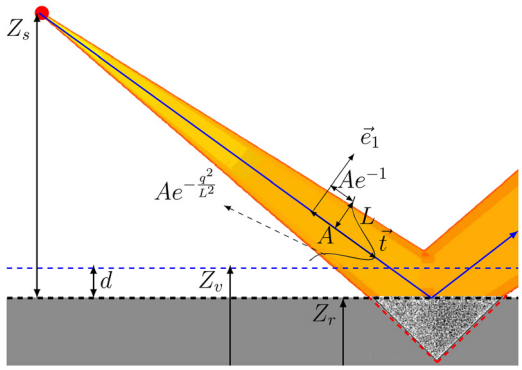

FIG. 3. (Color online) A sketch of a beam interacting with the terrain surface. The amplitude profile of the Gaussian beam along the trajectory of a straight ray and the ray-centered coordinates specified by the unit vector $\vec{t}$ tangent to the ray and the unit vector $\vec{e}_1$ normal to the ray. A indicates the beam amplitude on the central ray (blue line), and Ae^{-1} denotes the beam amplitude at the edge of the beam. The top boundary of the shaded area (black dashed line) represents the actual receiver line, while the dashed blue curve indicates the virtual line. The area inside the dashed triangle denotes the part of the beam that passes below the terrain surface.

and to carry out beam summation on a virtual surface or line $Z_v = Z_r + d$ instead of on the terrain surface (see Fig. 3). Here, d is defined as a function of the beam width $d = d(L(\boldsymbol{x}_r, \omega))$, $d < L(\boldsymbol{x}_r, \omega)$ and $d \to 0 if L(\boldsymbol{x}_r, \omega) \to 0$. In this case, one can not only satisfy the regularity condition of the ray field around the receivers but also account for the reflected wavefields as d will be defined in the vicinity of $\boldsymbol{x}_r$. Based on this observation, an expression of d can be sought in the form of $d = d(L(\boldsymbol{x}_r, \omega))$. As the beam width is a function of $\boldsymbol{M}$, it cannot be determined analytically without solving the DRT system. Furthermore, considering many receiver points at which the beam width can be different, it is not feasible to obtain a closed-form expression for d. Therefore, this study attempts to obtain a semi-empirical formulation through curve fitting.

In order to determine d, the impact of the wind and the inhomogeneity of the atmosphere on the wavefield on the terrain surfaces is assumed to be negligible. Hence, a 2D case with a homogeneous, quiescent atmosphere and a flat terrain is considered. For convenience, the acoustic wavelength $\lambda = c/f$ instead of the source frequency $f = \omega/2\pi$ is employed. The sound speed is $c = 340.3$ m/s and $f = [100, 3500]$ Hz. A time-harmonic monopole source is located at $(0, 5.28\lambda_0)$, here λ_0 is the wavelength corresponding to $f = 100$ Hz. Receivers $\boldsymbol{x}_r$ are distributed along the positive X-axis in a range $\bar{x} = [0, 14\lambda_0]$ with $0.14\lambda_0$ interval.

The beam width at $\boldsymbol{x}_r$ are calculated and the dependence of $L(\boldsymbol{x}_r, \omega)$ on ω and the range is illustrated in Fig. 4(a). As seen, $L(\boldsymbol{x}_r, \omega)$ increases considerably with increasing propagation range at lower frequencies. The increase in $L(\boldsymbol{x}_r, \omega)$ at a higher frequency is not so significant compared to the one at a lower frequency. To further analyze the dependence of $L(\boldsymbol{x}_r, \omega)$ on the frequency and the range, obtained $L(\boldsymbol{x}_r, \omega)$ values are normalized with their peak value of $L_{max} = 8.43$ m. Figure 4(b) depicts normalized beam width $L(\boldsymbol{x}_r, \omega)/L_{max}$ variation along the range at some frequencies. As seen, the variation along the range is almost linear; it is larger at the lower frequency and starts flattening when the frequency increases. Hence, one can state the relation as follows:

$$d = \mathcal{B}SD, \tag{20}$$

where $\mathcal{B}$ is the amplitude factor and here $\mathcal{B} = 1$ as normalized beam width of unit amplitude is considered, S is a dimensionless factor that describes the variation of the normalized beam width with respect to the frequency and the source-receiver distance D; hence, $S = S(D, \omega)$. The frequency dependence of the normalized beam width is illustrated in Fig. 4(c). At the receiver closer to the source location, the variation with the frequency is negligible, while the variation exhibits exponential behavior at longer ranges. By performing a curve fitting, an expression for S is obtained as

$$S = 1 - \exp\left(-\frac{0.1D/\lambda + 4\pi}{D/\lambda}\right). \tag{21}$$

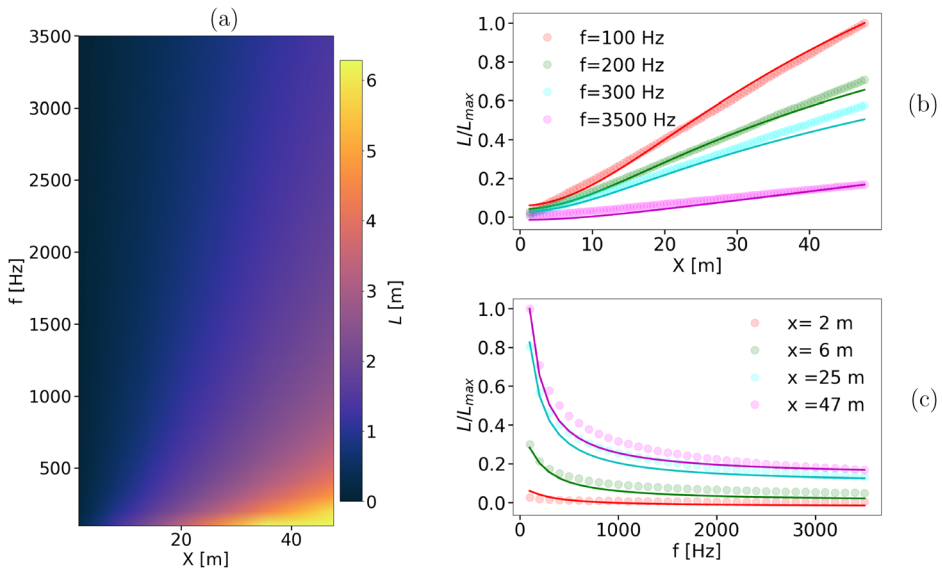

FIG. 4. (Color online) Beamwidth, L, as a function of source frequency and propagation range (a). Variation of the normalized beam width along the propagation range at some frequencies (b) and along the frequency at some receiver points (c). Filled circles indicate the data generated by the GBT tool, and solid lines represent the fitted curves.

https://doi.org/10.1121/10.0017825

A much better fit is obtained if D in Eq. (20) is replaced by $D - Z_s$. The fitted curves of d based on these expressions are depicted with the solid lines in Figs. 4(b) and 4(c). As seen, the curves fit well with the data points. In conclusion, since the parameter S in Eq. (20) has been determined by fitting the normalized beam width obtained with the GBT method, d can be interpreted as an offset that equals the beam width multiplied by the constant $\mathcal{B}$ ($\mathcal{B} < 1$).

The previous expression of d is obtained based on the normalized beam width of unit amplitude. Furthermore, the GBT solutions do not provide any information about $\mathcal{B}$ except $d < L(\boldsymbol{x}_r, \omega)$ and $d \to 0 if L(\boldsymbol{x}_r, \omega) \to 0$. Moreover, an essential criterion determining $\mathcal{B}$ is that the GBT results obtained with d should account for the reflected wavefields from buildings/obstacles on the terrain surface. Hence, the amplitude factor $\mathcal{B}$ must be determined by fitting the GBT solutions calculated using the expression of d with corresponding reference solutions. To this end, reference solutions are generated with a FEM-based reference solver considering the single-building urban configuration, which will be outlined in the following section. The amplitude factor $\mathcal{B}$ is found to be $\mathcal{B} = \pi/19$, which is obtained as the value that minimizes the error between the reference and GBT solutions for 45 GBT cases. These cases are generated considering sources in the frequency range [100, 150, 200 Hz] and locations [(50, 0, 5) m, (50, 5, 15) m,(50, 0, 18) m] and five values of B in the range [0, 1]. The final expression of d reads

$$d = \frac{\pi}{19}\left[1 - \exp\left(-\frac{0.1\zeta + 4\pi}{\zeta}\right)\right](D - Z_s), \tag{22}$$

where $\zeta = D/\lambda$.

III. VALIDATION CASE STUDY

The GBT model was assessed in the previous work of Fuerkaiti *et al.* (2021) by comparing it against an exact solution that describes the elementary sound propagation problem in a homogeneous atmosphere over flat terrain. In this work, the proposed semi-empirical formulation is validated against the FEM-based reference solution for different source frequencies and the source position. Then, the effect of 3D wind flow on acoustic propagation is investigated.

A. Reference solution

The reference solution is obtained using the frequency-domain FEM acoustic solver *Opty∂B*-GFD (Casalino *et al.*, 2009) and solving a second-order wave equation derived by Pierce (1990). The wave equation describes the propagation of potential fluctuations superimposed to a rotation mean flow that varies slowly over the length and time scales of the sound waves (high-frequency limit). *Opty∂B*-GFD uses an immersed boundary technique for automatic mesh generation. The immersed boundary method relies on the intrinsic capabilities of a finite-element scheme of decoupling the nodes at which the solution is calculated from the points where an equation is satisfied. Therefore, the zero-normal derivative equation of the perturbation velocity potential (slip condition) is satisfied at the exact points of the imported immersed geometry, using the exact value of the surface normal. In order to improve the capability of the method to take into account the diffraction of an edge, when one mesh volume element is crossed by a wedge, one or more mutually unconnected virtual nodes are added to the volume mesh by duplication, and an equal number of new equations are added to the system. Every additional equation corresponds to the slip condition with a local value of the surface normal. The FEM code *Opty∂B*-GFD has been validated for a variety of canonical problems (Casalino, 2010, 2012; Casalino *et al.*, 2009, 2012) involving acoustic propagation in uniform and non-uniform flows, and its complete description is outside the scope of the present work.

B. Case setup

Two different urban settings are considered. The urban setting with a single building block is used to validate the proposed semi-empirical formulation. At the same time, a three-building configuration is considered to study the acoustic effects of wind flow. All three building blocks have the same dimensions. The building length L_B is set to 4 m to keep the computational cost reasonable for the reference solution. The first two building blocks create the first urban canyon A, whose width is $4L_B$, and the second and third building blocks create the second urban canyon B, whose width is L_B. The urban boundary is considered to be a perfect reflector; hence no acoustic energy is absorbed by the boundaries. The dimensions of the computational domain and the building blocks are listed in Table. I.

A time-harmonic monopole source with two different source frequencies, i.e., 100 Hz, 200 Hz, and two different source locations, is considered. The source is stationary, and the source amplitude at a radial distance of 1 m from the source position is 0.2 Pa. The acoustic wavefield is studied on two different receiver planes: XZ-plane at $Y = 0$ m and XY-plane at $Z = 2.5\,L_B$. Building 1 is used to represent the single building configuration. Examples of source-receiver

TABLE I. Dimensions of the computational domain and building blocks.

Domain	x [m]	length [m]	y [m]	width [m]	z [m]	height [m]
Computational domain	[0, 60]	$15\,L_B$	[−10, 10]	$5L_B$	[0, 20]	$5L_B$
Building 1	[8, 12]	L_B	[−4, 4]	$2\,L_B$	[0, 12]	$3L_B$
Building 2	[28, 32]	L_B	[−4, 4]	$2\,L_B$	[0, 12]	$3L_B$
Building 3	[36, 40]	L_B	[−4, 4]	$2\,L_B$	[0, 12]	$3L_B$

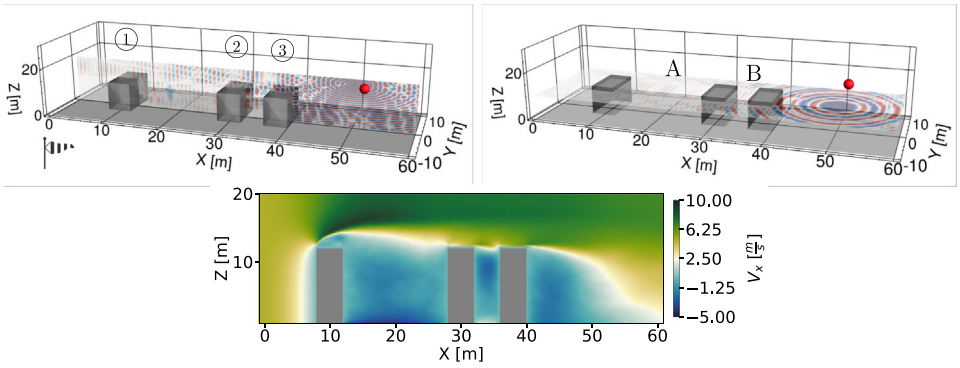

FIG. 5. (Color online) Source receiver geometry in a three-building environment. Vertical receiver plane at $Y = 0$ m (left). Horizontal receiver plane at $Z = 2.5L_B$ (right). Snapshot of the mean flow field on the vertical receiver plane (bottom). Wind direction points to the positive X-axis.

geometry for the three building configurations are displayed in Fig. 5.

For the given source frequencies, the perfectly matched layer (PML) thickness in the reference solution is set to $0.5\,L_B$ to prevent any contamination due to possible reflected waves from the domain boundaries and ensure the PML absorbs acoustic energy properly. Moreover, the domain is discretized by considering nine points per wavelength to ensure acceptable numerical accuracy.

In total, five cases that feature acoustic impacts of varying source frequencies, source-receiver geometries, urban settings, and weather conditions are considered to validate the present GBT model. The test matrix for this validation is listed in Table II. The GBT and the reference tools run on an Intel(R) Xeon(R) Gold 6140 CPU @2.3 GHz processor with 36 cores.

1. Weather conditions

Two weather conditions, a windy daytime and a quiescent daytime with a constant temperature of 15 °C ($c = 340.3$ m/s) are considered. The flow field in the computational domain is resolved using the high-fidelity computational fluid dynamics (CFD) solver SIMULIA PowerFLOW® (Dassault Systems, Vélizy-Villacoublay, France) based on the LB/VLES method, which is inherently unsteady and relies on an explicit time marching algorithm (Brès *et al.*, 2012; Casalino *et al.*, 2018; Kotapati *et al.*, 2009; Marié *et al.*, 2009; Shan *et al.*, 2006). One of the advantages of using PowerFLOW® for urban wind simulations is the full automation of the volume mesh generation, which is created by the software around the imported geometries by following user-defined regions of variable resolution (VR). A Cartesian mesh is employed by the lattice-Boltzmann scheme with a resolution jump of factor 2 between adjacent VRs. In every VR, the time marching algorithm uses a local time step, thus resulting in a rate that is twice faster in a twice finer resolution region. The calculation load is automatically balanced among processors based on the so-called fine-equivalent number of voxels, i.e., the number of voxels multiplied by the ratio between the local resolution and the maximum resolution level.

Three VRs are used, with the smallest voxel size of $0.0167L_B$. This results in a total voxel count of 72×10^6 within 70×10^6 fine-equivalent voxels. The VRs are placed in regions of interest, e.g., around the building edges. The initial velocity is set to 5 m/s at the inlet, and the wind direction points to the positive X-axis direction. The mean flow required by the GBT and reference calculations is then acquired by time-averaging flow data sampled at multiple time frames. A snapshot of the mean flowfield on the vertical receiver plane for the three-building configuration is displayed in Fig. 5. It should be noted that the mean flow profile may not fully represent the realistic wind profile as it is imposed only 8 m away from the first building.

C. Validation

1. Accuracy of the proposed semi-empirical formulation for the beam summation

The validity of the semi-empirical formulation, for varying source frequency, is evaluated by comparing the GBT predictions to the reference solutions in Case 1 and Case 2. Real values of the complex pressure and corresponding sound pressure levels (SPLs), calculated with and without the proposed empirical formulation, are compared to the reference results, as shown in Figs. 6 and 7.

TABLE II. Test matrix for the case study.

Case #	f [Hz]	Urban setting	Source location [m]	Receiver height [m]	Atmosphere
1	100	Single building	$(12.5, 1.25, 1.25)L_B$	0	Quiescent
2	200	Single building	$(12.5, 1.25, 1.25)L_B$	0	Quiescent
3	100	Single building	$(12.5, 0, 4.5)L_B$	0	Quiescent
4	200	Three buildings	$(12.5, 0, 4.5)L_B$	Receiver planes	Quiescent
5	200	Three buildings	$(12.5, 0, 4.5)L_B$	Receiver planes	Windy

https://doi.org/10.1121/10.0017825

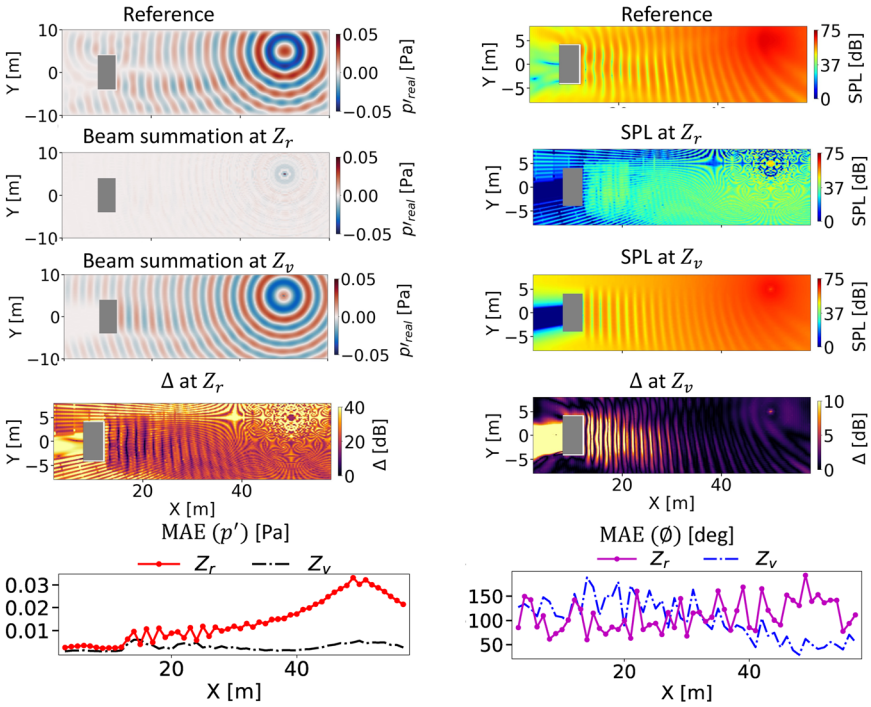

FIG. 6. (Color online) Comparison of the GBT with and without the semi-empirical formulation and the reference predictions on the terrain surface for Case 1: $f = 100$ Hz, source location $= (12.5, 1.25, 1.25)L_B$. The reference results are placed on the first row. The GBT results without the empirical formulation are presented in the second row and with the empirical formulation in the third row. AE in SPL without the empirical formulation is overlayed in the fourth row left and with the empirical formulation on the right. The MAE in pressure magnitude and phase are presented in the last row. This layout of results is maintained in the next two figures.

When the beam summation is performed without the proposed empirical formulation, i.e., on the terrain surface Z_r, the GBT predicts a very low-pressure magnitude due to the truncation error, as displayed in the second row of Fig. 6. A dramatic reduction of up to 40 dB is seen in the noise levels (see fourth row of Fig. 6). A remarkable improvement is achieved when the beam summation is performed with the proposed empirical formulation on the corresponding virtual surface at Z_v that captures well the general trend of the interference pattern of the reference result. The slight difference in the interference pattern is ascribed to the presence of diffraction in the reference solution, which is not included in the GBT model. To further highlight the improvement, mean absolute error (MAE) in pressure magnitude and phase and absolute error (AE) in the noise levels are calculated. The MAEs are evaluated at receiver points distributed along the X-axis with an $0.25L_B$ interval. At each point, an MAE is recorded by taking the mean value of the AEs sampled along the Y-axis with an $0.25L_B$ interval. The MAEs calculated with and without the empirical

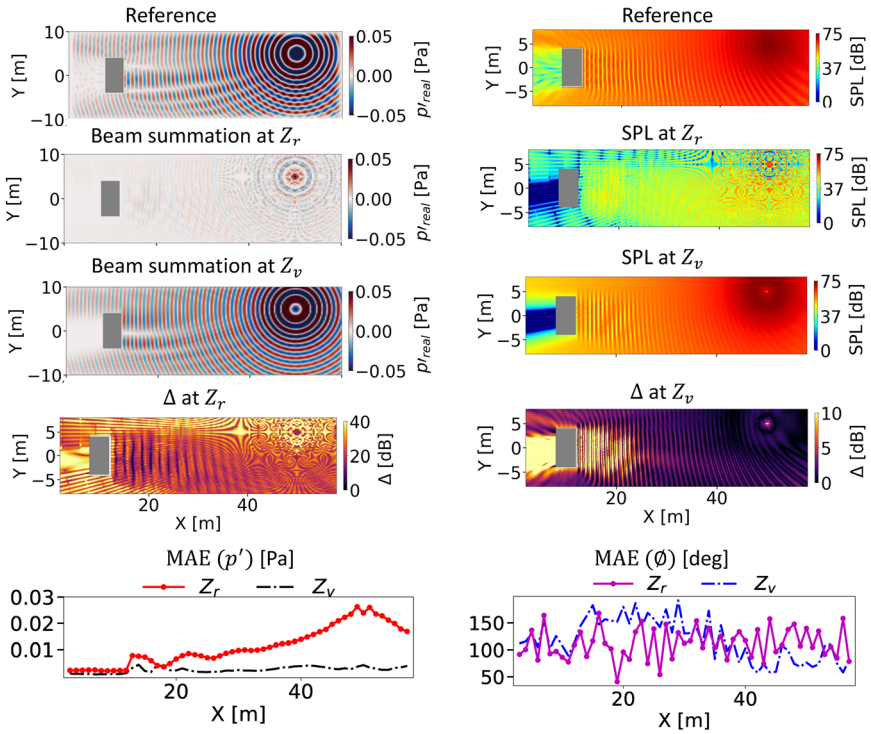

FIG. 7. (Color online) Comparison of the GBT with and without the semi-empirical formulation and the reference predictions on the terrain surface for Case 2: $f = 200$ Hz, source location $= (12.5, 1.25, 1.25)L_B$.

formulation are compared to each other. In Case 1, the maximum MAE of the pressure magnitude occurs around the source location and is reduced by an order of 2 with the proposed empirical formulation. The AE in the noise levels can reach up to 40 dB when the beam summation is performed on Z_r. While the beam summation is calculated on Z_v, the AE reduces greatly and is below 8 dB in the illuminated zone where direct rays can reach. Furthermore, the AE drops under 5 dB around the top and bottom sides of the building. This is attributed to the larger beam width of the limiting beam that separates the shadow and illuminated zones. Higher values of the AE behind the building are due to the lack of diffraction effects in the GBT model. The MAE of the phase calculated with the empirical formulation increases slightly in front of the building and reduces gradually at the receivers farther away from the building. A similar trend is observed in case 2. However, the AE around the top and bottom sides and the top left corner of the building increases noticeably more than in Case 1. This is due to the smaller beam width in Case 2 as a consequence of higher frequency; hence, the limiting beam cannot contribute more to the shadow zone behind the building.

The validity of the semi-empirical formulation under varying source locations is further examined by comparing the GBT predictions to the reference solutions in Cases 1 and 3. The results are displayed in Figs. 6 and 8, respectively. As seen from the field plots of the pressure magnitude and corresponding noise levels, for Case 3, the beam summation calculated on Z_r failed to approximate the reference solution. In contrast, the beam summation performed on Z_v can capture the general trend of the interference of the reference solution. The MAEs of the pressure magnitude calculated on both Z_r and Z_v get smaller than in Case 1. This is due to the higher source altitude, which improves the GBT prediction. For relatively lower frequency problems, the GBT method can give very satisfactory results if $Z_s - Z_r \gg \lambda$ so the beams can reflect properly (Porter, 2019). This has been discussed in ocean acoustics, and a validity condition is proposed as $Z_s - Z_r > 10\lambda$ (Jensen *et al.*, 2011). However, this has never been addressed in outdoor sound propagation problems. It remains unknown how small the wavelength should be with respect to the source altitude to ensure a satisfactory result. Further research is needed to investigate this aspect of the GBT method for outdoor sound propagation problems.

In general, the field predictions with the proposed semi-empirical formulation showed good agreement with the reference results. The proposed method can account for the reflected wavefields in the beam summation performed on the terrain surfaces for various source frequencies and locations and can be readily applied for outdoor sound propagation problems. However, it should also be noted that a smooth terrain surface is assumed in the derivation of the empirical formulation; therefore, it may fail when applied for receivers around the building corners. Moreover, it is noticed that the inclusion of the empirical formulation in the GBT calculations does not affect the CPU time. For the lower frequency (Cases 1 and 3), the CPU time of the reference and the GBT solver are comparable. However, for the higher frequency (Case 2), a 17-fold reduction in computation time is achieved with the GBT tool with respect to the reference solver.

2. Impact of 3D mean flow on the acoustic propagation

The present GBT model is validated against the reference solution for the three-building urban setting with and

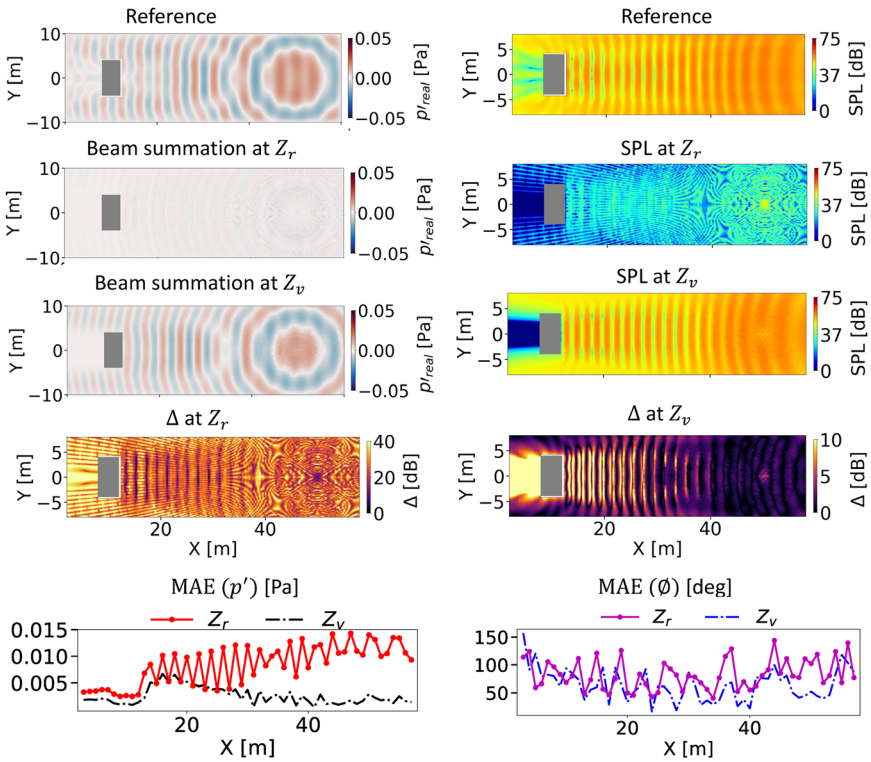

FIG. 8. (Color online) Comparison of the GBT with and without the semi-empirical formulation and the reference predictions on the terrain surface for Case 3: $f = 100$ Hz, source location $= (12.5, 0, 4.5)L_B$.

https://doi.org/10.1121/10.0017825

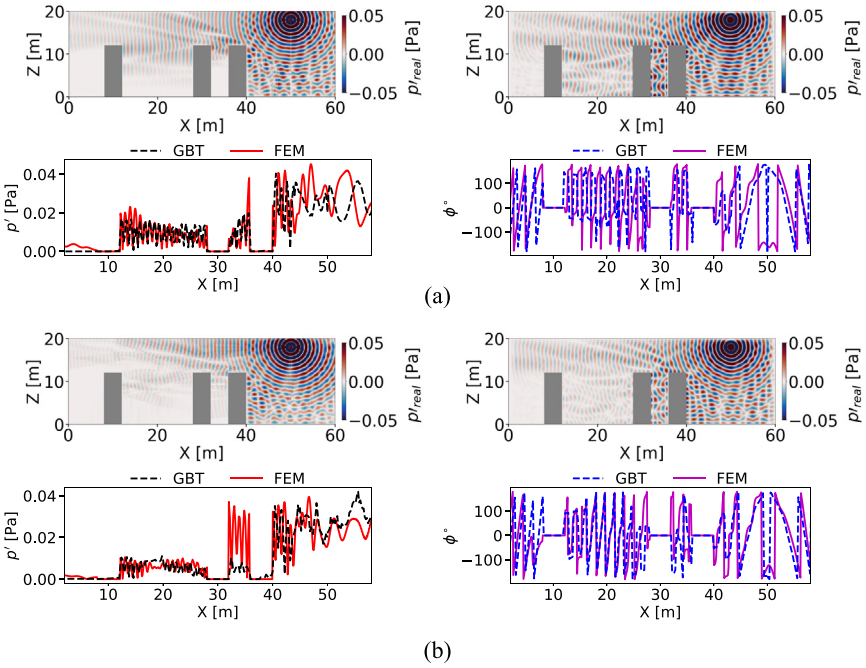

FIG. 9. (Color online) Comparison of the GBT and the reference solutions on the vertical receiver plane for Case 4 (a) and Case 5 (b). The first and third rows present the pressure field calculated with the GBT (left) and the reference (right) solvers. The second and fourth rows compare the pressure magnitude and the phase on a line Z $= 2.5L_B$ (10 m).

without the mean flow. The acoustic wavefields predicted with the GBT and the reference for Cases 4 and 5 are studied. The real values of the pressure field computed with the two approaches are compared at the vertical receiver plane and displayed in Fig. 9. In both cases, the GBT is able to capture the general trend of the reference result except inside the narrow canyon B, where the GBT predicts a smaller pressure amplitude than the reference solution. Nevertheless, a strong pressure oscillation is visible in the reference result due to diffraction and multiple reflections. A remarkable improvement in the GBT prediction is observed when comparing the line plots in Cases 4 and 5. In the presence of mean flow, the direct and reflected waves can have different ray paths than those in a quiescent medium. The phase increments along each path can change considerably, resulting in less apparent diffraction patterns and oscillations in the pressure amplitude. Furthermore, compared to Case 4, acoustic pressure amplitude in Case 5 drops in canyon A and rises in canyon B, highlighting the significant impact of different flow regimes inside urban canyons on acoustic propagation.

Figure 10 compares the predicted wavefields on the horizontal receiver plane. In the presence of the mean flow, the GBT approach can capture the general trend of the

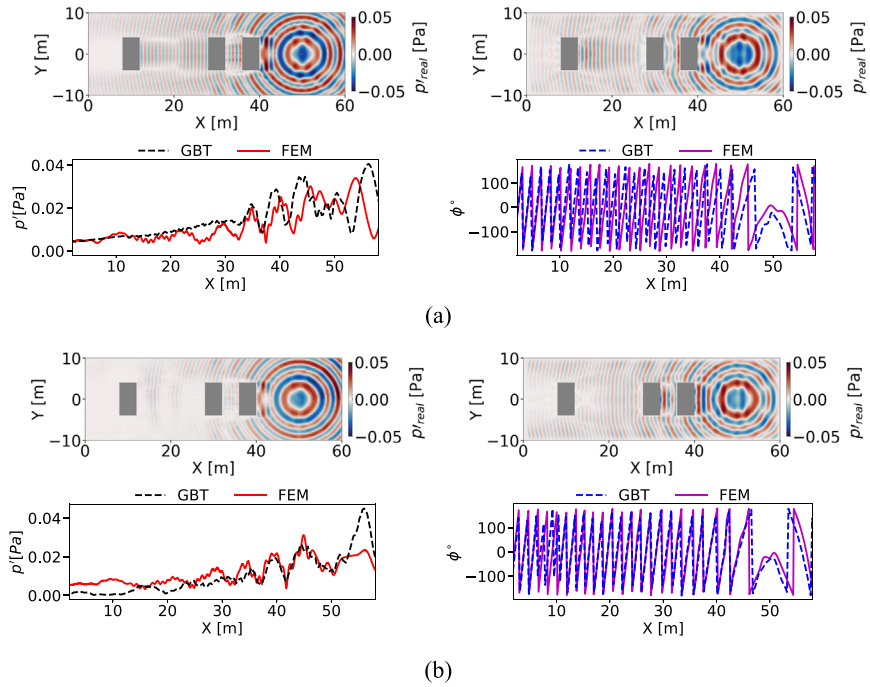

FIG. 10. (Color online) Comparison of the GBT and the reference solutions on the horizontal receiver plane for Case 4 (a) and Case 5 (b). The first and third rows present the pressure field calculated with the GBT (left) and the reference (right) solvers. The second and fourth rows compare the pressure magnitude and the phase on a line Y $= 1.75L_B$ (7 m).

interference pattern of the reference solution. However, the GBT predictions decay considerably at receivers located farther away from the source in the upstream direction and rise noticeably in the downstream direction. The line plot in Case 5 further highlights the impact of the mean flow on the diffraction pattern, particularly in terms of the phase of the complex pressure, as an excellent agreement is obtained.

IV. CONCLUSION

A new noise propagation approach is proposed to simulate airborne noise propagation in a non-turbulent urban environment with 3D varying terrain topology and weather conditions. The present GBT approach corrects the inconsistency between the RPT and the GBT equations presented in Gabillet *et al.* (1993) and establishes a complete framework for the GBT in an inhomogeneous moving atmosphere that accounts for the refraction due to vertical and horizontal variation in wind velocity and air temperature. A semi-empirical formulation is derived to reduce the truncation error in the beam summation and account for the reflected wavefields on the terrain surfaces. When the beam summation is performed without the empirical formulation, the maximum error is more than 40 dB due to the truncation error. In contrast, the agreement is improved significantly with the semi-empirical formulation, and the maximum error drops below 8 dB in the illuminated zone. The reflected wavefields on the terrain surface are also captured with a slight difference in the interference that is attributed to a lack of diffraction in the GBT model. The phase of the complex pressure showed excellent agreement with the reference data in the presence of wind flow, revealing the significant effect of the wind on the diffraction pattern. For the lower frequency, i.e., $f = 100$ Hz, the CPU time of both approaches are comparable. However, for the higher frequency, i.e., $f = 200$ Hz, a 17-fold reduction in computation time is achieved with the GBT tool with respect to the FEM solver.

The results suggest that the 3D wind flow should be accounted for when simulating airborne noise propagation in an urban environment. In the presence of mean flow, the direct and reflected waves can have different ray paths than those in a quiescent atmosphere. The phase increments along each path can change considerably, resulting in less apparent diffraction patterns and oscillations in the pressure amplitude. Furthermore, flow regimes inside urban canyons significantly impact acoustic propagation.

Some limitations in the present methodology should be recalled. The comparison with FEM provides a semi-quantitative validation, and any attempt to quantify the acoustic impact of various conditions is avoided because the Gaussian beam tracing approach presents an approximate solution of the wave equation. Furthermore, its accuracy threshold depends on the application (Beydoun and Ben-Menahem, 1985; Cervenỳ, 2001; Porter, 2019). Moreover, not even the FEM is an exact solution to the problems for two main reasons: First, it is a numerical solution affected by discretization error. Second, it is based on the solution of a second-order wave model for the acoustic velocity potential (Pierce, 1990), which may not describe the correct acoustic propagation in a highly sheared mean flow that would require the solution of the linearized Euler equation. The GBT approach in this work does not include diffraction effects. As the results demonstrated, more comprehensive models need to be developed to include the diffraction effects for lower frequency problems. Furthermore, the influence of atmospheric turbulence on propagation is ignored. More sophisticated models are needed to predict the wavefield in the shadow zones due to sound wave scattering by atmospheric turbulence.

ACKNOWLEDGMENTS

This work was financially supported by the Airbus Defence and Space GmbH.

Alguacil, A., Bauerheim, M., Jacob, M. C., and Moreau, S. (**2022**). "Deep learning surrogate for the temporal propagation and scattering of acoustic waves," AIAA J. **60**(10), 5890–5906.
Beydoun, W. B., and Ben-Menahem, A. (**1985**). "Range of validity of seismic ray and beam methods in general inhomogeneous media—II. A canonical problem," Geophys. J. Int **82**(2), 235–262.
Bian, H., Fattah, R., Zhong, S., and Zhang, X. (**2020**). "An efficient rectilinear Gaussian beam tracing method for sound propagation modelling in a non-turbulent medium," J. Acoust. Soc. Am. **148**(6), 4037–4048.
Bian, H., Fattah, R., Zhong, S., and Zhang, X. (**2021**). "On the efficient modeling of generic source directivity in Gaussian beam tracing," J. Acoust. Soc. Am. **149**(4), 2743–2751.
Bian, H., Tan, Q., Zhong, S., and Zhang, X. (**2022**). "Efficient computation of broadband noise propagation using Gaussian beam tracing method," J. Acoust. Soc. Am. **151**(5), 3387–3397.
Blumrich, R., and Heimann, D. (**2002**). "A linearized Eulerian sound propagation model for studies of complex meteorological effects," J. Acoust. Soc. Am. **112**(2), 446–455.
Brès, G. A., Freed, D., Wessels, M., Noelting, S., and Pérot, F. (**2012**). "Flow and noise predictions for the tandem cylinder aeroacoustic benchmark," Phys. Fluids **24**(3), 036101.
Casalino, D. (**2010**). "Reprint of: Benchmarking of different wave models for sound propagation in non-uniform flows," Procedia IUTAM **1**, 163–172.
Casalino, D. (**2012**). "Finite element solutions of a wave equation for sound propagation in sheared flows," AIAA J. **50**(1), 37–45.
Casalino, D., Barbarino, M., Genito, M., and Ferrara, V. (**2009**). "Hybrid empirical/computational aeroacoustics methodology for rocket noise modeling," AIAA J. **47**(6), 1445–1460.
Casalino, D., Barbarino, M., and Visingardi, A. (**2011**). "Simulation of helicopter community noise in complex urban geometry," AIAA J. **49**(8), 1614–1624.
Casalino, D., Hazir, A., and Mann, A. (**2018**). "Turbofan broadband noise prediction using the lattice Boltzmann method," AIAA J. **56**(2), 609–628.
Casalino, D., Santini, S., Genito, M., and Ferrara, V. (**2012**). "Rocket noise sources localization through a tailored beam-forming technique," AIAA J. **50**(10), 2146–2158.
Casalino, D., van der Velden, W. C., Romani, G., and Gonzalez-Martino, I. (**2019**). "Aeroacoustic analysis of urban air operations using the LB/VLES method," in *Proceedings of the 25th AIAA/CEAS Aeroacoustics Conference*, May 20–23, Delft, the Netherlands, p. 2662.
Cervenỳ, V. (**2001**). *Seismic Ray Theory*, 1st ed. (Cambridge University Press, Cambridge, UK).
Červenỳ, V., and Moser, T. J. (**2007**). "Ray propagator matrices in three-dimensional anisotropic inhomogeneous layered media," Geophys. J. Int. **168**(2), 593–604.

Červenỳ, V., and Pšenčík, I. (**2010**). "Gaussian beams in inhomogeneous anisotropic layered structures," Geophys. J. Int. **180**(2), 798–812.
Chessell, C. (**1973**). "Three-dimensional acoustic-ray tracing in an inhomogeneous anisotropic atmosphere using Hamilton's equations," J. Acoust. Soc. Am. **53**(1), 83–87.
Cotté, B., and Blanc-Benon, P. (**2009**). "Time-domain simulations of sound propagation in a stratified atmosphere over an impedance ground," J. Acoust. Soc. Am. **125**(5), EL202–EL207.
Doc, J.-B., Lihoreau, B., Félix, S., Faure, C., and Dubois, G. (**2015**). "Three-dimensional parabolic equation model for low frequency sound propagation in irregular urban canyons," J. Acoust. Soc. Am. **137**(1), 310–320.
Dragna, D., Blanc-Benon, P., and Poisson, F. (**2013**). "Time-domain solver in curvilinear coordinates for outdoor sound propagation over complex terrain," J. Acoust. Soc. Am. **133**(6), 3751–3763.
Franke, S. J., and Swenson, G., Jr. (**1989**). "A brief tutorial on the fast field program (FFP) as applied to sound propagation in the air," Appl. Acoust. **27**(3), 203–215.
Fuerkaiti, Y., Casalino, D., Avallone, F., and Ragni, D. (**2021**). "Toward inclusion of atmospheric effects in the aircraft community noise predictions," J. Acoust. Soc. Am. **150**(2), 759–768.
Gabillet, Y., Schroeder, H., Daigle, G. A., and L'Espérance, A. (**1993**). "Application of the Gaussian beam approach to sound propagation in the atmosphere: Theory and experiments," J. Acoust. Soc. Am. **93**(6), 3105–3116.
Gilbert, K. E., and Di, X. (**1993**). "A fast Green's function method for one-way sound propagation in the atmosphere," J. Acoust. Soc. Am. **94**(4), 2343–2352.
Gilbert, K. E., Raspet, R., and Di, X. (**1990**). "Calculation of turbulence effects in an upward-refracting atmosphere," J. Acoust. Soc. Am. **87**(6), 2428–2437.
Gilbert, K. E., and White, M. J. (**1989**). "Application of the parabolic equation to sound propagation in a refracting atmosphere," J. Acoust. Soc. Am. **85**(2), 630–637.
Heimann, D., and Karle, R. (**2006**). "A linearized Euler finite-difference time-domain sound propagation model with terrain-following coordinates," J. Acoust. Soc. Am. **119**(6), 3813–3821.
Hornikx, M. (**2004**). "Towards a parabolic equation for modeling urban sound propagation," in *Proceedings of the Long Range Sound Propagation Symposia*, June 1–3, Fairly, VT.
Hornikx, M., Dohmen, M., Conen, K., van Hooff, T., and Blocken, B. (**2018**). "The wind effect on sound propagation over urban areas: Predictions for generic urban sections," Build Environ. **144**, 519–531.
Jensen, F. B., Kuperman, W. A., Porter, M. B., Schmidt, H., and Tolstoy, A. (**2011**). *Computational Ocean Acoustics*, 2nd ed. (Springer, New York).
Klimeš, L. (**1994**). "Transformations for dynamic ray tracing in anisotropic media," Wave Motion **20**(3), 261–272.
Kotapati, R., Keating, A., Kandasamy, S., Duncan, B., Shock, R., and Chen, H. (**2009**). "The lattice-Boltzmann-VLES method for automotive fluid dynamics simulation, a review," Technical Report (SAE International, Warrendale, PA).
Marié, S., Ricot, D., and Sagaut, P. (**2009**). "Comparison between lattice Boltzmann method and Navier-Stokes high order schemes for computational aeroacoustics," J. Comput. Phys. **228**(4), 1056–1070.
Mo, Q., Yeh, H., Lin, M., and Manocha, D. (**2017**). "Outdoor sound propagation with analytic ray curve tracer and Gaussian beam," J. Acoust. Soc. Am. **141**(3), 2289–2299.
Moser, T. J., and Červenỳ, V. (**2007**). "Paraxial ray methods for anisotropic inhomogeneous media," Geophys. Prospect. **55**(1), 21–37.
Oshima, T., Imano, M., Hiraguri, Y., and Kamoshida, Y. (**2013**). "Linearized euler simulations of sound propagation with wind effects over a reconstructed urban terrain using digital geographic information," Appl. Acoust. **74**(12), 1354–1366.
Ostashev, V. E., and Wilson, D. K. (**2015**). *Acoustics in Moving Inhomogeneous Media*, 2nd ed. (CRC Press, Boca Raton, FL).
Ostashev, V. E., Wilson, D. K., Liu, L., Aldridge, D. F., Symons, N. P., and Marlin, D. (**2005**). "Equations for finite-difference, time-domain simulation of sound propagation in moving inhomogeneous media and numerical implementation," J. Acoust. Soc. Am. **117**(2), 503–517.
Papadakis, N. M., and Stavroulakis, G. E. (**2020**). "Finite element method for the estimation of insertion loss of noise barriers: Comparison with various formulae (2D)," Urban Sci. **4**(4), 77.
Pelat, A., Félix, S., and Pagneux, V. (**2009**). "On the use of leaky modes in open waveguides for the sound propagation modeling in street canyons," J. Acoust. Soc. Am. **126**(6), 2864–2872.
Pierce, A. D. (**1990**). "Wave equation for sound in fluids with unsteady inhomogeneous flow," J. Acoust. Soc. Am. **87**(6), 2292–2299.
Pierce, A. D. (**2019**). *Acoustics: An Introduction to Its Physical Principles and Applications*, 3rd ed. (Springer, New York).
Porter, M. B. (**2019**). "Beam tracing for two- and three-dimensional problems in ocean acoustics," J. Acoust. Soc. Am. **146**(3), 2016–2029.
Porter, M. B., and Bucker, H. P. (**1987**). "Gaussian beam tracing for computing ocean acoustic fields," J. Acoust. Soc. Am **82**(4), 1349–1359.
Raspet, R., Lee, S., Kuester, E., Chang, D., Richards, W., Gilbert, R., and Bong, N. (**1985**). "A fast-field program for sound propagation in a layered atmosphere above an impedance ground," J. Acoust. Soc. Am. **77**(2), 345–352.
Salomons, E. M. (**2001**). *Computational Atmospheric Acoustics* (Springer Science & Business Media, New York).
Salomons, E. M., Lohman, W. J., and Zhou, H. (**2016**). "Simulation of sound waves using the lattice Boltzmann method for fluid flow: Benchmark cases for outdoor sound propagation," PLoS ONE **11**(1), e0147206.
Shan, X., Yuan, X.-F., and Chen, H. (**2006**). "Kinetic theory representation of hydrodynamics: A way beyond the Navier–Stokes equation," J. Fluid Mech. **550**, 413–441.
Uginčius, P. (**1972**). "Ray acoustics and Fermat's principle in a moving inhomogeneous medium," J. Acoust. Soc. Am. **51**(5B), 1759–1763.
West, M., Gilbert, K., and Sack, R. (**1992**). "A tutorial on the parabolic equation (PE) model used for long range sound propagation in the atmosphere," Appl. Acoust. **37**(1), 31–49.
Wilson, D. K. (**1993**). "Sound field computations in a stratified, moving medium," J. Acoust. Soc. Am. **94**(1), 400–407.
Wilson, D. K., and Liu, L. (**2004**). "Finite-difference, time-domain simulation of sound propagation in a dynamic atmosphere," Technical Report (Defense Technical Information Center, Fort Belvoir, VA).
Zheng, Z. C., and Li, W. (**2008**). "Numerical stabilities and boundary conditions in time-domain eulerian simulations of acoustic wave propagations with and without background flow," J. Appl. Math. Comput. **202**(1), 146–161.